

Article

Aluminum Cation Doping in Ruddlesden-Popper Sr_2TiO_4 Enables High-Performance Photocatalytic Hydrogen Evolution

Jingsheng He ^{1,†}, Xiao Han ^{1,†}, Huimin Xiang ¹, Ran Ran ¹, Wei Wang ^{1,*}, Wei Zhou ¹ and Zongping Shao ^{2,*}

¹ State Key Laboratory of Materials-Oriented Chemical Engineering, College of Chemical Engineering, Nanjing Tech University, Nanjing 210009, China

² WA School of Mines: Minerals, Energy and Chemical Engineering, Curtin University, Perth, WA 6845, Australia

* Correspondence: wangwei@njtech.edu.cn (W.W.); zongping.shao@curtin.edu.au (Z.S.)

† These authors contributed equally to this work.

Abstract: Hydrogen (H_2) is regarded as a promising and renewable energy carrier to achieve a sustainable future. Among the various H_2 production routes, photocatalytic water splitting has received particular interest; it strongly relies on the optical and structural properties of photocatalysts such as their sunlight absorption capabilities, carrier transport properties, and amount of oxygen vacancy. Perovskite oxides have been widely investigated as photocatalysts for photocatalytic water splitting to produce H_2 because of their distinct optical properties, tunable band gaps and excellent compositional/structural flexibility. Herein, an aluminum cation (Al^{3+}) doping strategy is developed to enhance the photocatalytic performance of Ruddlesden-Popper (RP) Sr_2TiO_4 perovskite oxides for photocatalytic H_2 production. After optimizing the Al^{3+} substitution concentration, $\text{Sr}_2\text{Ti}_{0.9}\text{Al}_{0.1}\text{O}_4$ exhibits a superior H_2 evolution rate of $331 \mu\text{mol h}^{-1} \text{g}^{-1}$, which is ~ 3 times better than that of Sr_2TiO_4 under full-range light illumination, due to its enhanced light harvesting capabilities, facilitated charge transfer, and tailored band structure. This work presents a simple and useful Al^{3+} cation doping strategy to boost the photocatalytic performance of RP-phase perovskites for solar water splitting.

Keywords: Ruddlesden-Popper perovskite oxides; photocatalysis; hydrogen evolution; aluminum cation doping; water splitting



Citation: He, J.; Han, X.; Xiang, H.; Ran, R.; Wang, W.; Zhou, W.; Shao, Z. Aluminum Cation Doping in Ruddlesden-Popper Sr_2TiO_4 Enables High-Performance Photocatalytic Hydrogen Evolution. *Hydrogen* **2022**, *3*, 501–511. <https://doi.org/10.3390/hydrogen3040032>

Academic Editor: Salvador Eslava

Received: 6 November 2022

Accepted: 29 November 2022

Published: 1 December 2022

Publisher's Note: MDPI stays neutral with regard to jurisdictional claims in published maps and institutional affiliations.



Copyright: © 2022 by the authors. Licensee MDPI, Basel, Switzerland. This article is an open access article distributed under the terms and conditions of the Creative Commons Attribution (CC BY) license (<https://creativecommons.org/licenses/by/4.0/>).

1. Introduction

The energy crisis, greenhouse effect, and environmental issues caused by the overuse of fossil fuels have received increased attention recently. Thus, it is crucial to develop renewable and sustainable energy resources (e.g., wind, solar) and relevant technologies [1–3]. Solar energy is regarded as the most attractive renewable energy due to its abundance and clean nature; it can also be utilized by various routes [4–9]. Among them, photovoltaics and photocatalysis for the conversion of solar energy to fuels and electric power have received considerable attention for their efficient utilization of sunlight energy [10–15]. Principally, semiconductors used in photovoltaics directly transform solar energy to electricity, while semiconductors in photocatalysis enable the conversion from sunlight energy to chemical energy by means of photoinduced charge carriers for wastewater treatment and photocatalytic water splitting [10,12,13,16–20]. More importantly, photocatalysis is crucial in wastewater treatment and water splitting for hydrogen (H_2) production to address worldwide energy demands and environmental pollution [21–24]. H_2 is regarded as a highly promising energy carrier because clean water is only combustion product, while photocatalytic water splitting is considered one of the most promising methods of H_2 generation, and the photocatalytic efficiency is determined by the photocatalysts [25–28]. Consequently, it is crucial to develop cost-effective and earth-abundant photocatalysts with advanced water-splitting abilities [29–31].

At present, various types of photocatalysts have been designed and developed for photocatalytic water splitting, such as metal oxides, metal sulfides, carbon nitrides, etc. [32–35]. Simple metal oxides (e.g., TiO_2 and ZnO) have been extensively investigated in relation to

photocatalytic water splitting, showing relatively high photocatalytic activity [36,37]. Nevertheless, the performance of the reported simple oxide-based photocatalysts is significantly limited by their fixed atomic environment, wide band gap, and inferior stability, which limit their photocatalytic efficiency [38,39]. As a result, complex metal oxides are thought to be more applicable as high-performance photocatalysts because of their rich and tunable atomic environments, which exhibit easily tailored optical, chemical, and structural properties [40–44]. In particular, perovskite oxides, a significant class of complex oxides, have received increasing attention in relation to photocatalytic H₂ evolution reaction (HER) due to their easily tailored band gaps/structures, cost effectiveness, compositional/structural flexibility, and superior stability [12,40–42]. Additionally, the physical, optical, and electronic properties of conventional perovskites oxides (ABO₃) with three-dimensional structures can be effectively tuned by reducing the dimensions [12,40]. Notably, two-dimensional Ruddlesden-Popper (RP) perovskite oxides have gained increasing attention on account of their superior photocatalytic performance and unique chemical, structural, electronic, and optical features, as well as the fact that they play a promoting role in enhancing the separation and transportation of photo-induced charge carriers [45,46]. Sr₂TiO₄, a typical RP-phase perovskite, has been employed as a photocatalyst for water splitting and dye degradation, but exhibited inferior visible-light-driven photocatalytic performance because of the wide band gap of ~3.5 eV [46].

Functional doping is reported to be a useful and simple strategy to improve the photocatalytic performance of RP-phase Sr₂TiO₄ photocatalysts for solar water splitting by tuning the band structure/gap, charge transfer capability, and oxygen vacancy concentrations [47–49]. For instance, Xiao et al. reported a synergistic strategy by combining silver (Ag⁺) cation doping and reducing pretreatment to enhance the photocatalytic activity of Sr₂TiO₄ [47]. The optimized r-Ag_{0.05}Sr_{1.95}TiO₄, with a suitable amount of Ag⁺ cation substitution and reduced pretreatment, displayed a superior H₂ generation rate of 541 μmol h⁻¹ g⁻¹ under visible light illumination due to the enlarged specific surface area, the optimized band gap value, the enhanced light-harvesting capability, the presence of more surface oxygen vacancies, and reduced carrier recombination. In another work, Han et al. employed a fluorine (F⁻) anion doping strategy to boost the photocatalytic performance of Sr₂TiO₄ for H₂ production [48]. Sr₂TiO_{3.97}F_{0.03} with an optimized amount of F⁻ doping displayed outstanding H₂ production performance (282 μmol h⁻¹ g⁻¹) under full-range light irradiation, 44% higher than that of pristine Sr₂TiO₄, because of the increased amount of surface defect, the more strongly negative position of the conduction band, the reduced carrier recombination and well-balanced band gap value, the specific surface area, and the grain size. Nevertheless, the above-mentioned Ag⁺ and F⁻ doped Sr₂TiO₄ suffer from low doping concentrations of foreign ions (≤5 mol %), which may limit the improvement of the photocatalytic performance of Sr₂TiO₄. Meanwhile, metal cation doping with higher oxidation states (e.g., Rh⁴⁺) into RP-phase Sr₂TiO₄ competitively consumed photo-generated electrons, and played a detrimental role in the photocatalytic activity [50,51]. To solve the above-mentioned problems, we report a simple and useful strategy to increase the photocatalytic HER performance of Sr₂TiO₄ using a doping aluminum (Al³⁺) cation with a lower oxidation state and a higher doping concentration in the B-site of RP-phase Sr₂TiO₄.

Herein, we report a simple and useful strategy to increase the photocatalytic HER performance of Sr₂TiO₄ by doping an Al³⁺ cation into the B-site with higher doping concentrations. After optimizing the Al³⁺ doping concentration, Sr₂Ti_{0.9}Al_{0.1}O₄ demonstrated an increased photocatalytic H₂ production rate of 331 μmol h⁻¹ g⁻¹ under full-range light illumination (λ ≥ 250 nm), which was nearly three times better than that of Sr₂TiO₄, due to the reduced particle sizes, suppressed band gaps, stronger light harvesting capabilities, and improved separation and transfer capabilities of the photoinduced charge carriers. This study presents a new and efficient RP-type photocatalyst for high-efficiency water splitting, and provides insights that will enable the acceleration of large-scale applications of photocatalytic water splitting.

2. Materials and Methods

$\text{Sr}_2\text{Ti}_{1-x}\text{Al}_x\text{O}_4$ ($x = 0, 0.05, 0.1, \text{ and } 0.15$) with various Al^{3+} doping concentrations was prepared by the typical solid-state reaction route, using SrCO_3 , TiO_2 , and Al_2O_3 with different molar ratios as the precursors; these were mixed well in ethanol by 60-min high-energy ball milling. After drying, the mixed precursors were further annealed in air at $1000\text{ }^\circ\text{C}$ for 10 h to obtain the final photocatalysts. The phase structures, microstructures, and chemical states of various elements in the as-prepared photocatalysts were analyzed by X-ray diffraction (XRD, Bruker D8 Advance), field emission scanning electron microscopy (FE-SEM, Hitachi S4800), and with an XPS spectrometer (Thermo ESCALAB 250), respectively. The energy dispersive X-ray spectrometer (EDX) was used to investigate the elemental compositions of various samples. The Autosorb-iQ3 instrument was employed to measure the Brunauer–Emmett–Teller (BET) surface areas of various samples. The ultraviolet-visible (UV-vis) spectrophotometer (Lambda 750S) and FL 6500 photoluminescence (PL) spectrometer were employed to measure the diffuse reflectance spectra and fluorescence emission of the as-prepared photocatalysts, respectively. The photocatalytic performance of various photocatalysts was determined using a photocatalytic performance evaluation instrument (CEL-PAEMD8, China Education Au-light); detailed information regarding this process can be found in our previous work [48].

A three-electrode system was used to investigate the photoelectrochemical properties of photocatalysts in a $0.1\text{ M Na}_3\text{PO}_4/\text{Na}_2\text{HPO}_4$ aqueous solution ($\text{pH} = 7.9$) under full-range light irradiation on a CHI760E workstation. The photocatalyst powder-based slurries were spin-coated on F^- doped tin oxide (FTO) glass to serve as the working electrode [48], while Ag/AgCl and Pt functioned as the reference and counter electrodes, respectively. Cyclic voltammetry of 50 cycles at a scan rate of 200 mV s^{-1} was used to activate the working electrode. After that, the linear sweep voltammetry (LSV) curves were obtained at a scan rate of 10 mV s^{-1} and a voltage range of $-1.6\text{--}0\text{ V}$. Nyquist plots of various photocatalysts were obtained using electrochemical impedance spectroscopy (EIS) at -1.2 V under light irradiation with frequencies in the range of $0.1\text{--}10^5\text{ Hz}$, using the CHI760E workstation.

3. Results and Discussion

Generally, a high calcination temperature ($\geq 1000\text{ }^\circ\text{C}$) is required for the synthesis of Sr_2TiO_4 using the solid-state reaction route, due to the high energy barrier of SrO layer intercalation into the SrTiO_3 with an ABO_3 structure [45]. Figure 1 shows the XRD patterns of various Sr_2TiO_4 samples with different Al^{3+} doping amounts calcined at $1000\text{ }^\circ\text{C}$; the main diffraction peaks of the four samples are consistent with the peaks of RP-type Sr_2TiO_4 (JCPDS No. 00-039-1471), suggesting that Al^{3+} doping had no obvious impact on the phase structure of Sr_2TiO_4 . It was found that the main peaks ($31^\circ \leq 2\theta \leq 33^\circ$) of the $\text{Sr}_2\text{Ti}_{1-x}\text{Al}_x\text{O}_4$ samples exhibited shifts to higher 2θ values, as compared with the pristine Sr_2TiO_4 in Figure 1, implying that the Al^{3+} cation with a smaller ionic radius (0.535 \AA) than that of Ti^{4+} (0.605 \AA) and Ti^{3+} (0.67 \AA) cations was successfully doped in the lattice of RP-phase Sr_2TiO_4 with a lattice contraction [52,53]. Nevertheless, when the doping ratio of the Al^{3+} cation was higher than 0.1, an $\text{Sr}_4\text{Ti}_3\text{O}_{10}$ (JCPDS: No. 00-022-1444) impurity phase appeared in the $\text{Sr}_2\text{Ti}_{0.85}\text{Al}_{0.15}\text{O}_4$ sample, which may have a detrimental effect on photocatalytic activity [54].

The microstructures, particle sizes, and elemental distributions of Al^{3+} -doped Sr_2TiO_4 were investigated using SEM and EDX elemental mapping, which showed a significant effect on the photocatalytic performance. SEM images and the corresponding grain size histograms are provided in Figure 2a–d. It seems that the particles of various Sr_2TiO_4 -based photocatalysts exhibited irregular shapes, with particle size distributions in the range of $150\text{--}300\text{ nm}$. Although the Al^{3+} doping efficiently decreased the particle sizes of the pristine Sr_2TiO_4 photocatalyst, the more serious particle agglomeration inevitably reduced the BET specific surface areas, as shown in Figures S1 and S2 and Table S1. Furthermore, the corresponding EDX elemental mapping image in Figure 3 illustrates the well-distributed

Sr, Ti, and O elements in pristine Sr_2TiO_4 and Sr, Ti, Al, and O elements in $\text{Sr}_2\text{Ti}_{0.9}\text{Al}_{0.1}\text{O}_4$, further confirming that Al^{3+} cations were successfully doped in the lattice of Sr_2TiO_4 .

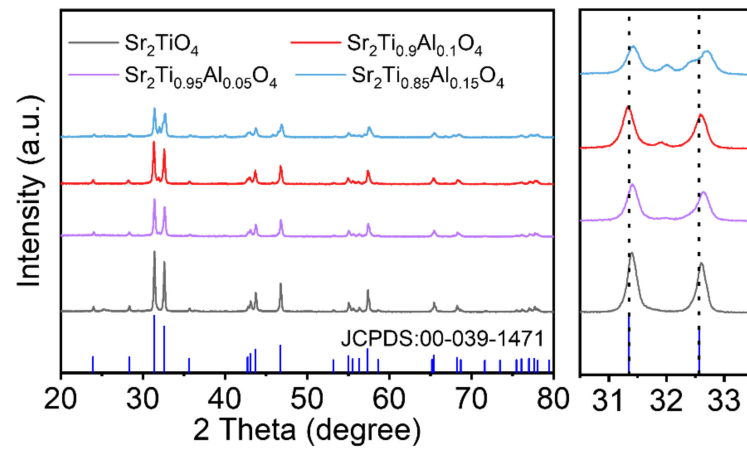


Figure 1. XRD patterns of $\text{Sr}_2\text{Ti}_{1-x}\text{Al}_x\text{O}_4$ ($x = 0, 0.05, 0.1$ and 0.15).

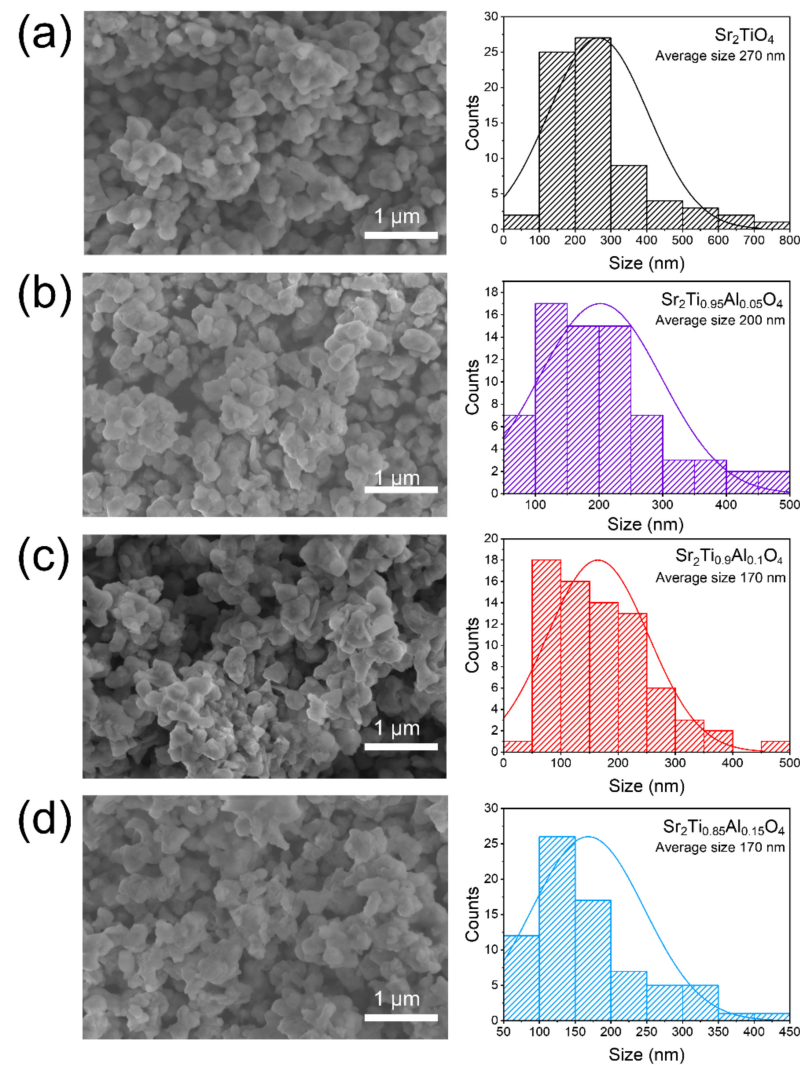


Figure 2. SEM images and the corresponding grain-size histograms of (a) Sr_2TiO_4 , (b) $\text{Sr}_2\text{Ti}_{0.95}\text{Al}_{0.05}\text{O}_4$, (c) $\text{Sr}_2\text{Ti}_{0.9}\text{Al}_{0.1}\text{O}_4$, and (d) $\text{Sr}_2\text{Ti}_{0.85}\text{Al}_{0.15}\text{O}_4$.

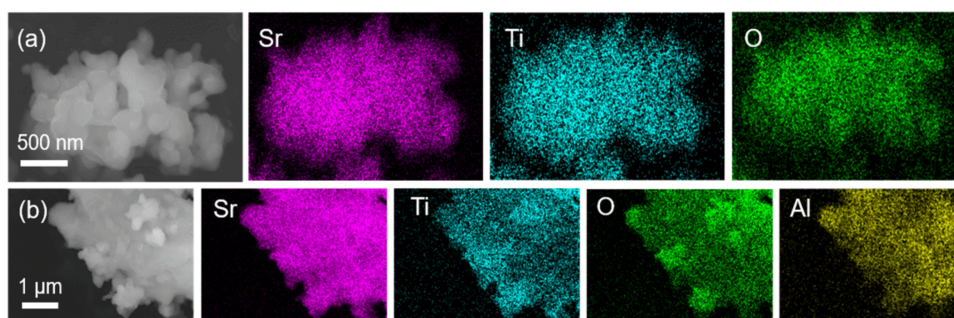


Figure 3. SEM-EDX images of (a) Sr_2TiO_4 and (b) $\text{Sr}_2\text{Ti}_{0.9}\text{Al}_{0.1}\text{O}_4$. This is a figure. Schemes follow the same formatting.

The XPS technique was employed to investigate the influence of Al^{3+} doping on the chemical states of various elements in Sr_2TiO_4 , with results shown in Figures 4 and S2. As depicted in Figure 4a, all samples exhibited two main peaks at binding energy (BE) positions of around 458.0 and 464.0 eV in Ti 2p XPS spectra, corresponding to Ti 2p_{3/2} and Ti 2p_{1/2}, respectively [55]. As compared with pristine Sr_2TiO_4 , the Ti XPS peaks of the Al^{3+} doped samples shifted to the lower BE positions, demonstrating the formation of Ti^{3+} cations induced by the Al^{3+} doping. In addition, O 1s XPS spectra were mainly composed of four peaks at BEs of around 530.1, 531.1, 532.0, and 533.2 eV, representing the lattice oxygen, $\text{O}_2^{2-}/\text{O}^-$ species, the surface-absorbed hydroxyl groups/oxygen ($-\text{OH}/\text{O}_2$), and absorbed carbonates/water on the surface ($\text{CO}_3^{2-}/\text{H}_2\text{O}$), respectively [56]. In fact, the content of surface oxygen vacancy as a crucial factor in determining the photocatalytic performance was closely tied to the $\text{O}_2^{2-}/\text{O}^-$ species [57]. It can be seen that the number of $\text{O}_2^{2-}/\text{O}^-$ species for $\text{Sr}_2\text{Ti}_{0.9}\text{Al}_{0.1}\text{O}_4$ was much higher than those of the other four samples, implying the highest amount of surface oxygen vacancies. Based on the Al 2p XPS spectra in Figure 4c, the intensity of the typical peak for Al at a BE of around 74 eV was gradually increased with the increase in the Al^{3+} doping concentration from 0.05 to 0.10, suggesting that the Al^{3+} cations of suitable amounts were successfully doped into the lattice of Sr_2TiO_4 .

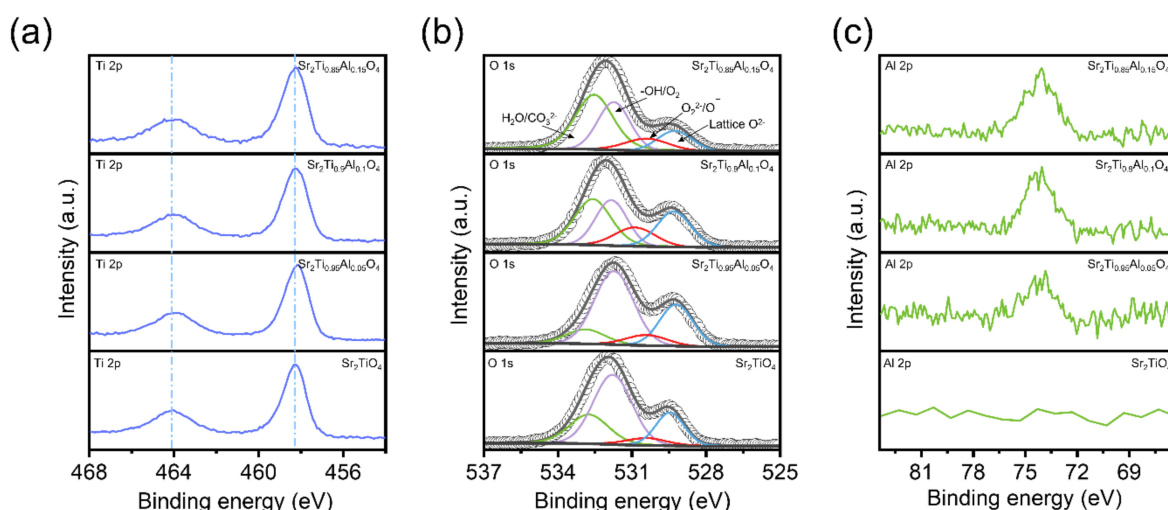


Figure 4. XPS spectra of $\text{Sr}_2\text{Ti}_{1-x}\text{Al}_x\text{O}_4$ ($x = 0, 0.05, 0.1, \text{ and } 0.15$): (a) Ti 2p, (b) O 1s, and (c) Al 2p.

Besides the phase structure and morphology, the light-harvesting capability of the photocatalyst is another decisive factor for photocatalytic HER activity [47]. UV-vis spectra were used to identify the impact of Al^{3+} substitution amounts on the sunlight-harvesting capabilities of Sr_2TiO_4 . As depicted in Figure 5a, all samples exhibited strong light absorption in the ultraviolet (UV) region. Moreover, the increase in the Al^{3+} doping concentration from 0 to 0.10 in Sr_2TiO_4 gradually led to improved light absorption capabilities at higher

wavelengths because of the reduced band gaps. In addition, $\text{Sr}_2\text{Ti}_{0.9}\text{Al}_{0.1}\text{O}_4$ exhibited a stronger absorbance intensity and light harvesting capability than $\text{Sr}_2\text{Ti}_{0.85}\text{Al}_{0.15}\text{O}_4$ at wavelengths larger than 375 nm. Although $\text{Sr}_2\text{Ti}_{0.85}\text{Al}_{0.15}\text{O}_4$ exhibited stronger absorbance intensity at wavelengths from 340–375 nm, the inferior photocatalytic performance of $\text{Sr}_2\text{Ti}_{0.85}\text{Al}_{0.15}\text{O}_4$, compared to that of $\text{Sr}_2\text{Ti}_{0.9}\text{Al}_{0.1}\text{O}_4$, was mainly attributed to the reduced specific surface area, wider band gap, larger charge transfer resistance and the existence of $\text{Sr}_4\text{Ti}_3\text{O}_{10}$ impurity. The Kubelka–Munk transformation displayed in Figure 5b was employed to obtain the band gap energies (E_g) of various Sr_2TiO_4 photocatalysts. Sr_2TiO_4 displayed an E_g of 3.32 eV, agreeing well with the reported E_g for Sr_2TiO_4 in previous investigations [58]. For Al^{3+} -doped Sr_2TiO_4 , decreased E_g values of 3.20, 3.06, and 3.16 eV were observed for $\text{Sr}_2\text{Ti}_{0.95}\text{Al}_{0.05}\text{O}_4$, $\text{Sr}_2\text{Ti}_{0.9}\text{Al}_{0.1}\text{O}_4$, and $\text{Sr}_2\text{Ti}_{0.85}\text{Al}_{0.15}\text{O}_4$, respectively, as displayed in Figure 5b and Table S1; these results suggest that the Al^{3+} doping is effective in narrowing the band gap of Sr_2TiO_4 . Notably, $\text{Sr}_2\text{Ti}_{0.9}\text{Al}_{0.1}\text{O}_4$ exhibited the lowest E_g with much-enhanced light-harvesting capability, which was beneficial for improving the photocatalytic activity.

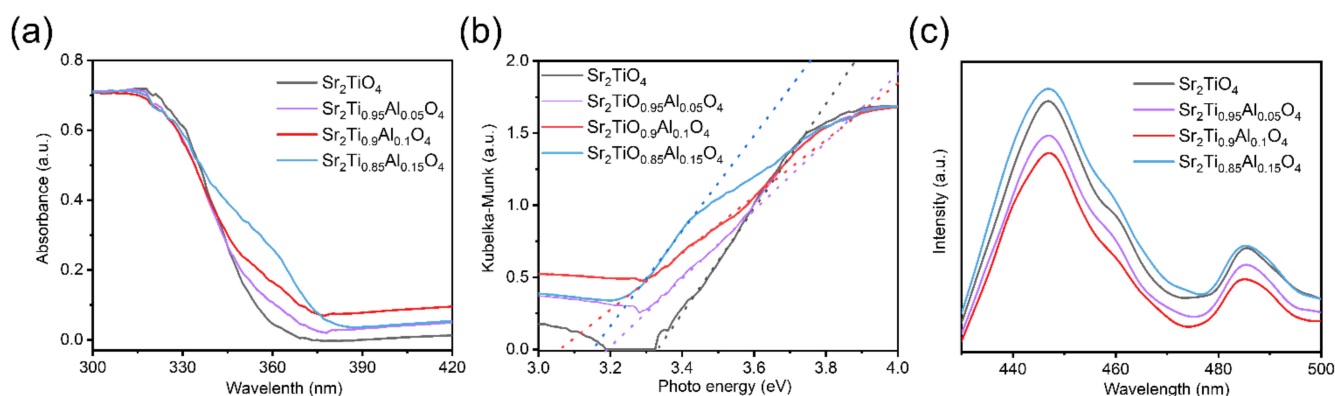


Figure 5. (a) UV-vis diffuse reflectance spectra, (b) Kubelka–Munk curves and (c) PL spectra of $\text{Sr}_2\text{Ti}_{1-x}\text{Al}_x\text{O}_4$ ($x = 0, 0.05, 0.1, \text{ and } 0.15$).

It has been widely reported that the separation, transport, and recombination behaviors of photogenerated charge carriers play crucial roles in the photocatalytic activity of photocatalysts, which can be characterized using the PL technique [59]. The PL spectra of the Sr_2TiO_4 and various Al^{3+} doped Sr_2TiO_4 are displayed in Figure 5c. Under excitation at a wavelength of 380 nm, all of the investigated samples exhibited emission peaks at a wavelength range of 420–550 nm. As compared with Sr_2TiO_4 , $\text{Sr}_2\text{Ti}_{0.95}\text{Al}_{0.05}\text{O}_4$ and $\text{Sr}_2\text{Ti}_{0.9}\text{Al}_{0.1}\text{O}_4$ showed lower PL emission peak intensities, indicating the facilitated separation and transport capabilities of the charge carriers. Nevertheless, $\text{Sr}_2\text{Ti}_{0.85}\text{Al}_{0.15}\text{O}_4$ with excessive Al^{3+} doping exhibited a higher PL emission peak intensity than that of pristine Sr_2TiO_4 because of the inhibited separation and transport of photoexcited carriers induced by the existence of the impurity phase in $\text{Sr}_2\text{Ti}_{0.85}\text{Al}_{0.15}\text{O}_4$.

The photocatalytic activities of the as-prepared $\text{Sr}_2\text{Ti}_{1-x}\text{Al}_x\text{O}_4$ ($x = 0, 0.05, 0.1, \text{ and } 0.15$) photocatalysts were evaluated by testing the H_2 production amounts in a mixed $\text{Na}_2\text{SO}_3/\text{Na}_2\text{S}$ aqueous solution under full-range light irradiation, in which Na_2SO_3 and Na_2S functioned as sacrificial agents to react with the photoinduced holes. Figure 6a displays steady and continuous H_2 production during photocatalytic water splitting under full-range light illumination, and the H_2 production rates of all samples are presented in Figure 6b. $\text{Sr}_2\text{Ti}_{1-x}\text{Al}_x\text{O}_4$ ($x = 0, 0.05, 0.1, \text{ and } 0.15$) exhibited better photocatalytic HER activity than pristine Sr_2TiO_4 , demonstrating the effectiveness of Al^{3+} doping in boosting the photocatalytic activity. Notably, $\text{Sr}_2\text{Ti}_{0.9}\text{Al}_{0.1}\text{O}_4$ exhibited the maximum H_2 evolution rate (of $331 \mu\text{mol h}^{-1} \text{g}^{-1}$) among the three Al^{3+} doped samples, which was nearly three times higher than that of the undoped Sr_2TiO_4 ($85 \mu\text{mol h}^{-1} \text{g}^{-1}$) due to the enhanced light-harvesting capabilities, suppressed carrier recombination, and reduced E_g value. In

addition, $\text{Sr}_2\text{Ti}_{0.85}\text{Al}_{0.15}\text{O}_4$ with excessive amounts of Al^{3+} doping exhibited an inferior H_2 generation rate to that of $\text{Sr}_2\text{Ti}_{0.9}\text{Al}_{0.1}\text{O}_4$ due to the inhibited separation and transport of photoinduced carriers and the large E_g value. As for the photocatalytic stability of HER, the $\text{Sr}_2\text{Ti}_{0.9}\text{Al}_{0.1}\text{O}_4$ photocatalyst exhibited steady and continuous H_2 production for 15 h (Figure 7a). The amount of H_2 produced with $\text{Sr}_2\text{Ti}_{0.9}\text{Al}_{0.1}\text{O}_4$ was measured to $82.6 \mu\text{mol}$ in the first 5 h, and the initial H_2 production rate was $328 \mu\text{mol h}^{-1} \text{g}^{-1}$. In addition, the H_2 evolution amount was increased to $219.8 \mu\text{mol}$ after 15 h of operation and the average H_2 evolution rate was $292 \mu\text{mol h}^{-1} \text{g}^{-1}$, which was nearly 90% of the initial value after 15 h of continuous operation (Figure 7a). As compared with the sample before the photocatalytic reaction, the $\text{Sr}_2\text{Ti}_{0.9}\text{Al}_{0.1}\text{O}_4$ photocatalyst exhibited no obvious changes in the phase structure and particle sizes after the stability test under full-range light illumination, as depicted in Figure 7b,d,e. As shown in Figure 7c, the cycling performance of $\text{Sr}_2\text{Ti}_{0.9}\text{Al}_{0.1}\text{O}_4$ photocatalyst was determined by testing the HER rates in three cycles. The $\text{Sr}_2\text{Ti}_{0.9}\text{Al}_{0.1}\text{O}_4$ photocatalyst exhibited a high recyclability without any obvious degradation in the HER rates ($\sim 297 \mu\text{mol h}^{-1} \text{g}^{-1}$).

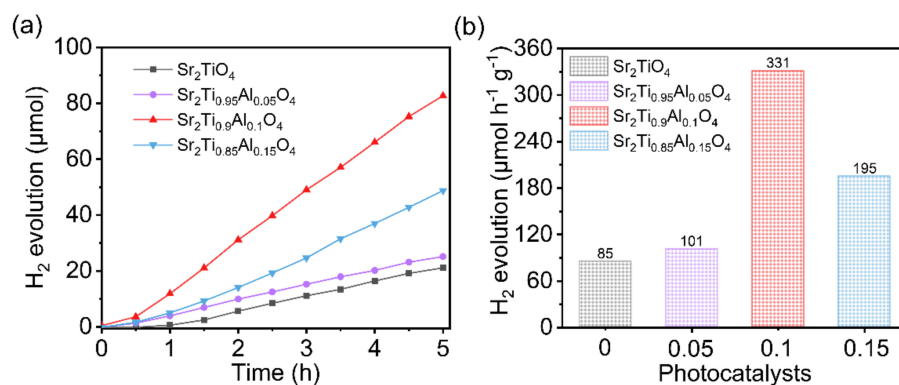


Figure 6. (a) H_2 evolution amounts and (b) average H_2 evolution rates of $\text{Sr}_2\text{Ti}_{1-x}\text{Al}_x\text{O}_4$ ($x = 0, 0.05, 0.1$, and 0.15) samples under full-range sunlight illumination.

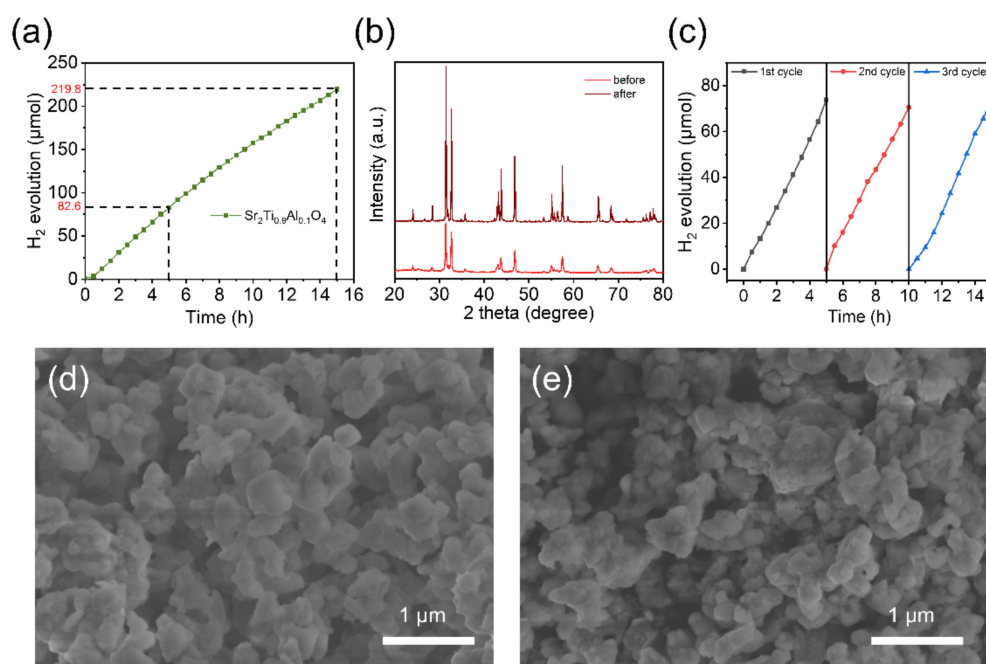


Figure 7. (a) H_2 production amounts of $\text{Sr}_2\text{Ti}_{0.9}\text{Al}_{0.1}\text{O}_4$ in a continuous test period of 15 h. (b) XRD patterns of $\text{Sr}_2\text{Ti}_{0.9}\text{Al}_{0.1}\text{O}_4$ before and after the stability test. (c) Recycling tests of $\text{Sr}_2\text{Ti}_{0.9}\text{Al}_{0.1}\text{O}_4$ for photocatalytic HER. SEM images of $\text{Sr}_2\text{Ti}_{0.9}\text{Al}_{0.1}\text{O}_4$ (d) before and (e) after the stability test.

The LSV curves of various $\text{Sr}_2\text{Ti}_{1-x}\text{Al}_x\text{O}_4$ ($x = 0, 0.05, 0.1, \text{ and } 0.15$) photocatalysts were measured under full-range light illumination to further verify the enhanced photocatalytic activity of $\text{Sr}_2\text{Ti}_{0.9}\text{Al}_{0.1}\text{O}_4$. As depicted in Figure 8a, after the cyclic voltammetry activation, the photocatalysts showed similar onset potential for the cathodic current. In addition, $\text{Sr}_2\text{Ti}_{0.9}\text{Al}_{0.1}\text{O}_4$ exhibited larger current densities than those of Sr_2TiO_4 , $\text{Sr}_2\text{Ti}_{0.95}\text{Al}_{0.05}\text{O}_4$, and $\text{Sr}_2\text{Ti}_{0.85}\text{Al}_{0.15}\text{O}_4$, demonstrating the superior photocatalytic HER activity of $\text{Sr}_2\text{Ti}_{0.9}\text{Al}_{0.1}\text{O}_4$. Based on the EIS results in Figure 8b, the $\text{Sr}_2\text{Ti}_{0.9}\text{Al}_{0.1}\text{O}_4$ photocatalysts exhibited the smallest charge transfer resistance among the four investigated samples due to the suppressed recombination of photogenerated carriers, as evidenced by the PL results, which were consistent with the photocatalytic HER activities of various photocatalysts under irradiation.

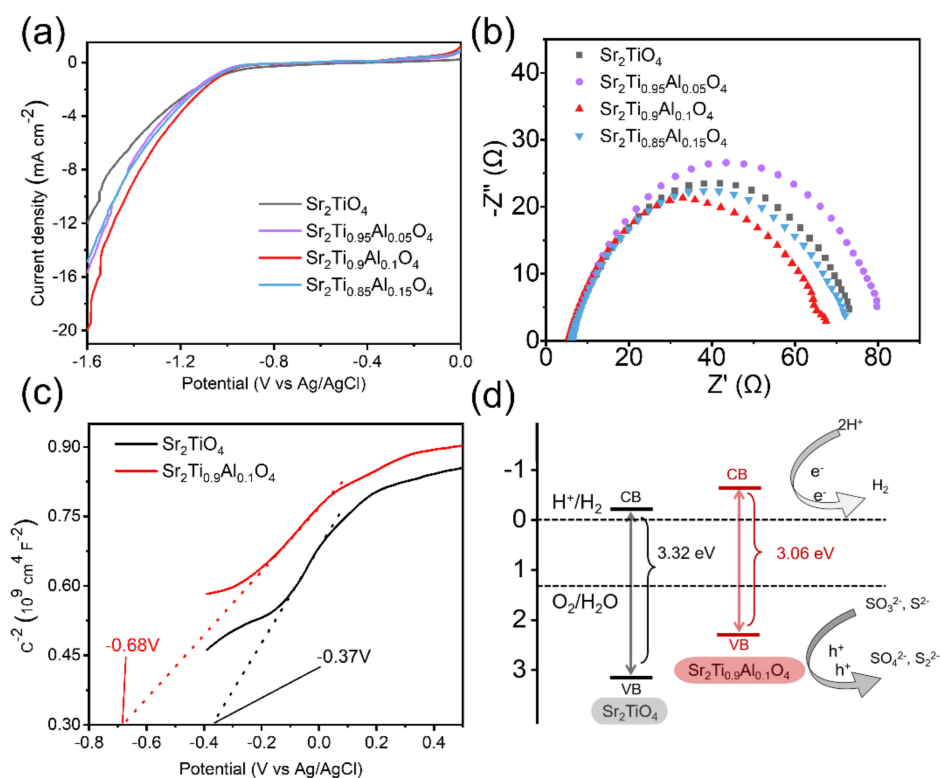


Figure 8. (a) LSV curves and (b) EIS spectra of $\text{Sr}_2\text{Ti}_{1-x}\text{Al}_x\text{O}_4$ ($x = 0, 0.05, 0.1, \text{ and } 0.15$). (c) MS curves and (d) schematically illustrated band structures of Sr_2TiO_4 and $\text{Sr}_2\text{Ti}_{0.9}\text{Al}_{0.1}\text{O}_4$.

Mott–Schottky curves were further tested to measure the energy band positions, including the conduction bands (CB) and the valence bands (VB) of the Sr_2TiO_4 and $\text{Sr}_2\text{Ti}_{0.9}\text{Al}_{0.1}\text{O}_4$ photocatalysts. As shown in Figure 8c, the flat band potentials of the photocatalysts can be acquired by extrapolating the Mott–Schottky curves to the X-axis. It can be observed that the flat band positions of Sr_2TiO_4 and $\text{Sr}_2\text{Ti}_{0.9}\text{Al}_{0.1}\text{O}_4$ were measured to be -0.37 and -0.68 eV (vs. Ag/AgCl), respectively. Thus, the CB edges of Sr_2TiO_4 and $\text{Sr}_2\text{Ti}_{0.9}\text{Al}_{0.1}\text{O}_4$ were calculated to be -0.17 and -0.48 eV (vs. the normal hydrogen electrode, NHE), respectively. Based on the E_g values measured by the Kubelka–Munk transformation, the VB edges of Sr_2TiO_4 and $\text{Sr}_2\text{Ti}_{0.9}\text{Al}_{0.1}\text{O}_4$ were calculated to be 3.15 and 2.58 eV (vs. NHE), respectively. Based on the schematic diagrams of the band structures of Sr_2TiO_4 and $\text{Sr}_2\text{Ti}_{0.9}\text{Al}_{0.1}\text{O}_4$, as shown in Figure 8d, it seems that the Al^{3+} doping effectively regulated the band positions of Sr_2TiO_4 . The CB edge of $\text{Sr}_2\text{Ti}_{0.9}\text{Al}_{0.1}\text{O}_4$, which was more strongly negative than that of the pristine Sr_2TiO_4 , enabled a much higher driving force of the photoexcited electrons for water reduction, and led to a significant enhancement of the photocatalytic HER performance of Sr_2TiO_4 .

4. Conclusions

In conclusion, we successfully fabricated several $\text{Sr}_2\text{Ti}_{1-x}\text{Al}_x\text{O}_4$ ($x = 0, 0.05, 0.1,$ and 0.15) photocatalysts using a conventional solid-state reaction method. The $\text{Sr}_2\text{Ti}_{0.9}\text{Al}_{0.1}\text{O}_4$ photocatalyst exhibited the most outstanding photocatalytic HER activity ($331 \mu\text{mol h}^{-1} \text{g}^{-1}$) among the three investigated Al^{3+} -doped Sr_2TiO_4 photocatalysts under full-range light irradiation, which was nearly three times higher than that of Sr_2TiO_4 . Such a remarkable improvement in the photocatalytic performance of Sr_2TiO_4 induced by Al^{3+} doping was attributed to the reduced particle sizes, enhanced light harvesting capability, facilitated charge transfer, and tailored band structure. Furthermore, $\text{Sr}_2\text{Ti}_{0.9}\text{Al}_{0.1}\text{O}_4$ also exhibited good stability and recyclability for photocatalytic HER. In sum, this study reports a highly promising catalyst ($\text{Sr}_2\text{Ti}_{0.9}\text{Al}_{0.1}\text{O}_4$) for photocatalytic water splitting, which may contribute to the further development of perovskite-based photocatalysts for efficient solar conversion.

Supplementary Materials: The following supporting information can be downloaded at: <https://www.mdpi.com/article/10.3390/hydrogen3040032/s1>, Figure S1: N_2 adsorption and desorption curves of $\text{Sr}_2\text{Ti}_{1-x}\text{Al}_x\text{O}_4$ ($x = 0, 0.05, 0.1,$ and 0.15); Figure S2. Sr 3d XPS spectra of $\text{Sr}_2\text{Ti}_{1-x}\text{Al}_x\text{O}_4$ ($x = 0, 0.05, 0.1,$ and 0.15); Table S1. BET specific surface areas and band gap energies of various $\text{Sr}_2\text{Ti}_{1-x}\text{Al}_x\text{O}_4$ samples ($x = 0, 0.05, 0.1,$ and 0.15).

Author Contributions: Investigation, formal analysis, visualization, writing—original draft, data curation, validation, J.H.; investigation, formal analysis, data curation, X.H.; data curation, H.X.; writing—review and editing, R.R.; supervision, conceptualization, writing—review and editing, funding acquisition, W.W.; project administration, funding acquisition, W.Z.; supervision, writing—review and editing, funding acquisition, Z.S. All authors have read and agreed to the published version of the manuscript.

Funding: This work was supported by the National Natural Science Foundation of China (No. 22279057) and the Postgraduate Research and Practice Innovation Program of Jiangsu Province (No. KYCX22_1352).

Institutional Review Board Statement: Not applicable.

Informed Consent Statement: Not applicable.

Data Availability Statement: The data that support the findings of this study are available from the corresponding author upon reasonable request.

Conflicts of Interest: The authors declare no conflict of interest.

References

1. Østergaard, P.A.; Duic, N.; Noorollahi, Y.; Mikulcic, H.; Kalogirou, S. Sustainable development using renewable energy technology. *Renew. Energy* **2020**, *146*, 2430–2437. [[CrossRef](#)]
2. Razmjoo, A.; Gakenia Kaigutha, L.; Vaziri Rad, M.A.; Marzband, M.; Davarpanah, A.; Denai, M. A technical analysis investigating energy sustainability utilizing reliable renewable energy sources to reduce CO_2 emissions in a high potential area. *Renew. Energy* **2021**, *164*, 46–57. [[CrossRef](#)]
3. Saavedra, M.M.R.; de O. Fontes, C.H.; Freires, M.F.G. Sustainable and renewable energy supply chain: A system dynamics overview. *Renew. Sust. Energy Rev.* **2018**, *82*, 247–259. [[CrossRef](#)]
4. Kannan, N.; Vakeesan, D. Solar energy for future world: A review. *Renew. Sust. Energy Rev.* **2016**, *62*, 1092–1105. [[CrossRef](#)]
5. Mekhilef, S.; Saidur, R.; Safari, A. A review on solar energy use in industries. *Renew. Sust. Energy Rev.* **2011**, *15*, 1777–1790. [[CrossRef](#)]
6. Gong, J.; Li, C.; Wasielewski, M.R. Advances in solar energy conversion. *Chem. Soc. Rev.* **2019**, *48*, 1862–1864. [[CrossRef](#)]
7. Rabaia, M.K.H.; Abdelkareem, M.A.; Sayed, E.T.; Elsaid, K.; Chae, K.J.; Wilberforce, T.; Olabi, A.G. Environmental impacts of solar energy systems: A review. *Sci. Total Environ.* **2021**, *754*, 141989. [[CrossRef](#)]
8. Solangi, K.H.; Islam, M.R.; Saidur, R.; Rahim, N.A.; Fayaz, H. A review on global solar energy policy. *Renew. Sust. Energy Rev.* **2011**, *15*, 2149–2163. [[CrossRef](#)]
9. Tosti, S.; Pozio, A.; Farina, L.; Santucci, A. Hydrogen and oxygen production via water splitting in a solar-powered membrane reactor—A conceptual study. *Hydrogen* **2021**, *2*, 18–32. [[CrossRef](#)]
10. He, J.; Liu, P.; Ran, R.; Wang, W.; Zhou, W.; Shao, Z. Single-atom catalysts for high-efficiency photocatalytic and photoelectrochemical water splitting: Distinctive roles, unique fabrication methods and specific design strategies. *J. Mater. Chem. A* **2022**, *10*, 6835–6871. [[CrossRef](#)]

11. Huang, D.; Xiang, H.; Ran, R.; Wang, W.; Zhou, W.; Shao, Z. Recent advances in nanostructured inorganic hole-transporting materials for perovskite solar cells. *Nanomaterials* **2022**, *12*, 2592. [[CrossRef](#)] [[PubMed](#)]
12. Wang, W.; Xu, M.; Xu, X.; Zhou, W.; Shao, Z. Perovskite oxide based electrodes for high-performance photoelectrochemical water Splitting. *Angew. Chem. Int. Ed.* **2020**, *59*, 136–152. [[CrossRef](#)] [[PubMed](#)]
13. Xiang, H.; Liu, P.; Ran, R.; Wang, W.; Zhou, W.; Shao, Z. Two-dimensional Dion-Jacobson halide perovskites as new-generation light absorbers for perovskite solar cells. *Renew. Sust. Energy Rev.* **2022**, *166*, 112614. [[CrossRef](#)]
14. Yang, X.; Wang, W.; Ran, R.; Zhou, W.; Shao, Z. Recent advances in Cs₂AgBiBr₆-based halide double perovskites as lead-free and inorganic light absorbers for perovskite solar cells. *Energy Fuels* **2020**, *34*, 10513–10528. [[CrossRef](#)]
15. Takata, T.; Jiang, J.; Sakata, Y.; Nakabayashi, M.; Shibata, N.; Nandal, V.; Seki, K.; Hisatomi, T.; Domen, K. Photocatalytic water splitting with a quantum efficiency of almost unity. *Nature* **2020**, *581*, 411–414. [[CrossRef](#)] [[PubMed](#)]
16. Ren, G.; Han, H.; Wang, Y.; Liu, S.; Zhao, J.; Meng, X.; Li, Z. Recent advances of photocatalytic application in water treatment: A review. *Nanomaterials* **2021**, *11*, 1804. [[CrossRef](#)]
17. Saeed, M.; Muneer, M.; Haq, A.; Akram, N. Photocatalysis: An effective tool for photodegradation of dyes—A review. *Environ. Sci. Pollut. Res.* **2022**, *29*, 293–311. [[CrossRef](#)]
18. Wu, Y.; Zhong, L.; Yuan, J.; Xiang, W.; Xin, X.; Liu, H.; Luo, H.; Li, L.; Chen, M.; Zhong, D.; et al. Photocatalytic optical fibers for degradation of organic pollutants in wastewater: A review. *Environ. Chem. Lett.* **2021**, *19*, 1335–1346. [[CrossRef](#)]
19. Xiang, H.; Liu, P.; Wang, W.; Ran, R.; Zhou, W.; Shao, Z. Sodium fluoride sacrificing layer concept enables high-efficiency and stable methylammonium lead iodide perovskite solar cells. *J. Mater. Sci. Technol.* **2022**, *113*, 138–146. [[CrossRef](#)]
20. Yang, X.; Xiang, H.; Huang, J.; Zhou, C.; Ran, R.; Wang, W.; Zhou, W.; Shao, Z. Thiourea with sulfur-donor as an effective additive for enhanced performance of lead-free double perovskite photovoltaic cells. *J. Colloid Interface Sci.* **2022**, *628*, 476–485. [[CrossRef](#)]
21. Ahmad, K.; Ghatak, H.R.; Ahuja, S.M. A review on photocatalytic remediation of environmental pollutants and H₂ production through water splitting: A sustainable approach. *Environ. Technol. Innov.* **2020**, *19*, 100893. [[CrossRef](#)]
22. Nasir, A.M.; Awang, N.; Jaafar, J.; Ismail, A.F.; Othman, M.H.D.; Rahman, M.A.; Aziz, F.; Yajid, M.A.M. Recent progress on fabrication and application of electrospun nanofibrous photocatalytic membranes for wastewater treatment: A review. *J. Water Process. Eng.* **2021**, *40*, 101878. [[CrossRef](#)]
23. Riaz, S.; Park, S.-J. An overview of TiO₂-based photocatalytic membrane reactors for water and wastewater treatments. *J. Ind. Eng. Chem.* **2020**, *84*, 23–41. [[CrossRef](#)]
24. Yao, S.; Yuan, X.; Jiang, L.; Xiong, T.; Zhang, J. Recent progress on fullerene-based materials: Synthesis, properties, modifications, and photocatalytic applications. *Materials* **2020**, *13*, 2924. [[CrossRef](#)]
25. Fajrina, N.; Tahir, M. A critical review in strategies to improve photocatalytic water splitting towards hydrogen production. *Int. J. Hydrogen Energy* **2019**, *44*, 540–577. [[CrossRef](#)]
26. Liu, X.; Chi, J.; Dong, B.; Sun, Y. Recent progress in decoupled H₂ and O₂ production from electrolytic water splitting. *ChemElectroChem* **2019**, *6*, 2157–2166. [[CrossRef](#)]
27. Miseki, Y.; Sayama, K. Photocatalytic water splitting for solar hydrogen production using the carbonate effect and the Z-Scheme reaction. *Adv. Energy Mater.* **2019**, *9*, 1801294. [[CrossRef](#)]
28. Zhang, Q.; Guan, J. Recent progress in single-atom catalysts for photocatalytic water splitting. *Sol. RRL* **2020**, *4*, 2000283. [[CrossRef](#)]
29. Hu, C.; Lin, Y.-R.; Yang, H.-C. Recent developments in graphitic carbon nitride based hydrogels as photocatalysts. *ChemSusChem* **2019**, *12*, 1794–1806. [[CrossRef](#)]
30. Li, Y.; Song, X.; Zhang, G.; Wang, L.; Liu, Y.; Chen, W.; Chen, L. 2D covalent organic frameworks toward efficient photocatalytic hydrogen evolution. *ChemSusChem* **2022**, *15*, e202200901. [[CrossRef](#)]
31. Wang, Z.; Li, C.; Domen, K. Recent developments in heterogeneous photocatalysts for solar-driven overall water splitting. *Chem. Soc. Rev.* **2019**, *48*, 2109–2125. [[CrossRef](#)] [[PubMed](#)]
32. Reddy, C.V.; Reddy, K.R.; Shetti, N.P.; Shim, J.; Aminabhavi, T.M.; Dionysiou, D.D. Hetero-nanostructured metal oxide-based hybrid photocatalysts for enhanced photoelectrochemical water splitting—A review. *Int. J. Hydrogen Energy* **2020**, *45*, 18331–18347. [[CrossRef](#)]
33. Han, Y.; Chen, Y.; Fan, R.; Li, Z.; Zou, Z. Promotion effect of metal phosphides towards electrocatalytic and photocatalytic water splitting. *EcoMat* **2021**, *3*, e12097. [[CrossRef](#)]
34. Lin, L.; Yu, Z.; Wang, X. Crystalline carbon nitride semiconductors for photocatalytic water splitting. *Angew. Chem. Int. Ed.* **2019**, *58*, 6164–6175. [[CrossRef](#)] [[PubMed](#)]
35. Soto Morillo, E.; Mota Toledo, N.; García Fierro, J.L.; Navarro Yerga, R.M. Role of the sulphur source in the solvothermal synthesis of Ag-CdS photocatalysts: Effects on the structure and photoactivity for hydrogen production. *Hydrogen* **2020**, *1*, 64–89. [[CrossRef](#)]
36. Singh, R.; Dutta, S. A review on H₂ production through photocatalytic reactions using TiO₂/TiO₂-assisted catalysts. *Fuel* **2018**, *220*, 607–620. [[CrossRef](#)]
37. Hamid, S.B.A.; Teh, S.J.; Lai, C.W. Photocatalytic water oxidation on ZnO: A review. *Catalysts* **2017**, *7*, 93. [[CrossRef](#)]
38. Guo, Q.; Zhou, C.; Ma, Z.; Yang, X. Fundamentals of TiO₂ photocatalysis: Concepts, mechanisms, and challenges. *Adv. Mater.* **2019**, *31*, 1901997. [[CrossRef](#)]
39. Kumaravel, V.; Mathew, S.; Bartlett, J.; Pillai, S.C. Photocatalytic hydrogen production using metal doped TiO₂: A review of recent advances. *Appl. Catal. B Environ.* **2019**, *244*, 1021–1064. [[CrossRef](#)]

40. Grabowska, E. Selected perovskite oxides: Characterization, preparation and photocatalytic properties-A review. *Appl. Catal. B Environ.* **2016**, *186*, 97–126. [[CrossRef](#)]
41. Kumar, A.; Kumar, A.; Krishnan, V. Perovskite oxide based materials for energy and environment-oriented photocatalysis. *ACS Catal.* **2020**, *10*, 10253–10315. [[CrossRef](#)]
42. Rodionov, I.A.; Zvereva, I.A. Photocatalytic activity of layered perovskite-like oxides in practically valuable chemical reactions. *Russ. Chem. Rev.* **2016**, *85*, 248–279. [[CrossRef](#)]
43. Abdi, F.F.; Berglund, S.P. Recent developments in complex metal oxide photoelectrodes. *J. Phys. D Appl. Phys.* **2017**, *50*, 193002. [[CrossRef](#)]
44. Liu, Y.; Yang, B.; He, H.; Yang, S.; Duan, X.; Wang, S. Bismuth-based complex oxides for photocatalytic applications in environmental remediation and water splitting: A review. *Sci. Total Environ.* **2022**, *804*, 150215. [[CrossRef](#)]
45. Hu, Y.; Mao, L.; Guan, X.; Tucker, K.A.; Xie, H.; Wu, X.; Shi, J. Layered perovskite oxides and their derivative nanosheets adopting different modification strategies towards better photocatalytic performance of water splitting. *Renew. Sust. Energy Rev.* **2020**, *119*, 109527. [[CrossRef](#)]
46. Xiao, H.; Liu, P.; Wang, W.; Ran, R.; Zhou, W.; Shao, Z. Ruddlesden-Popper perovskite oxides for photocatalysis-based water splitting and wastewater treatment. *Energy Fuels* **2020**, *34*, 9208–9221. [[CrossRef](#)]
47. Xiao, H.; Liu, P.; Wang, W.; Ran, R.; Zhou, W.; Shao, Z. Enhancing the photocatalytic activity of Ruddlesden-Popper Sr₂TiO₄ for hydrogen evolution through synergistic silver doping and moderate reducing pretreatment. *Mater. Today Energy* **2022**, *23*, 100899. [[CrossRef](#)]
48. Han, X.; Liu, P.; Ran, R.; Wang, W.; Zhou, W.; Shao, Z. Non-metal fluorine doping in Ruddlesden-Popper perovskite oxide enables high-efficiency photocatalytic water splitting for hydrogen production. *Mater. Today Energy* **2022**, *23*, 100896. [[CrossRef](#)]
49. Hu, C.; Chen, T.-S.; Huang, H.-X. Heterojunction of n-type Sr₂TiO₄ with p-type Bi₅O₇I with enhanced photocatalytic activity under irradiation of simulated sunlight. *Appl. Surf. Sci.* **2017**, *426*, 536–544. [[CrossRef](#)]
50. Sun, X.; Xu, X. Efficient photocatalytic hydrogen production over La/Rh co-doped Ruddlesden-Popper compound Sr₂TiO₄. *Appl. Catal. B Environ.* **2017**, *210*, 149–159. [[CrossRef](#)]
51. Konta, R.; Ishii, T.; Kato, H.; Kudo, A. Photocatalytic activities of noble metal ion doped SrTiO₃ under visible light irradiation. *J. Phys. Chem. B* **2004**, *108*, 8992–8995. [[CrossRef](#)]
52. Mao, M.M.; Chen, X.M.; Liu, X.Q. Structure and microwave dielectric properties of solid solution in SrLaAlO₄-Sr₂TiO₄ System. *J. Am. Ceram. Soc.* **2011**, *94*, 3948–3952. [[CrossRef](#)]
53. Zhang, J.; Xie, K.; Li, Y.; Qi, W.; Ruan, C.; Wu, Y. Composite cathode based on Mn-doped perovskite niobate-titanate for efficient steam electrolysis. *Chin. J. Chem. Phys.* **2014**, *27*, 457–464. [[CrossRef](#)]
54. Noguera, C. Theoretical investigation of the Ruddlesden-Popper compounds Sr_{n+1}Ti_nO_{3n+1} (n = 1–3). *Philos. Mag. Lett.* **2000**, *80*, 173–180. [[CrossRef](#)]
55. Sun, X.; Mi, Y.; Jiao, F.; Xu, X. Activating layered perovskite compound Sr₂TiO₄ via La/N codoping for visible light photocatalytic water splitting. *ACS Catal.* **2018**, *8*, 3209–3221. [[CrossRef](#)]
56. Shang, P.; Ye, Z.; Ding, Y.; Zhu, Z.; Peng, X.; Ma, G.; Li, D. Nanosponge-like solid solution of NiMo with a high hydrogen evolution reaction performance over a wide range of current densities. *ACS Sustain. Chem. Eng.* **2020**, *8*, 10664–10672. [[CrossRef](#)]
57. She, S.; Yu, J.; Tang, W.; Zhu, Y.; Chen, Y.; Sunarso, J.; Zhou, W.; Shao, Z. Systematic study of oxygen evolution activity and stability on La_{1-x}Sr_xFeO_{3-δ} perovskite electrocatalysts in alkaline media. *ACS Appl. Mater. Interfaces* **2018**, *10*, 11715–11721. [[CrossRef](#)]
58. Kwak, B.S.; Do, J.Y.; Park, N.K.; Kang, M. Surface modification of layered perovskite Sr₂TiO₄ for improved CO₂ photoreduction with H₂O to CH₄. *Sci. Rep.* **2017**, *7*, 16370. [[CrossRef](#)]
59. Jing, L.; Qu, Y.; Wang, B.; Li, S.; Jiang, B.; Yang, L.; Fu, W.; Fu, H.; Sun, J. Review of photoluminescence performance of nano-sized semiconductor materials and its relationships with photocatalytic activity. *Sol. Energy Mater. Sol. Cells* **2006**, *90*, 1773–1787.